

1 **Revision 1**

2 **Compression and Structure of Brucite to 31 GPa from Synchrotron X-ray**
3 **Diffraction and Infrared Spectroscopy Studies**

4 Maining Ma^{1,2}, Wei Liu¹, Zhiqiang Chen³, Zhenxian Liu⁴, Baosheng Li^{1,*}

5
6 ¹Mineral Physics Institute, Stony Brook University, Stony Brook, NY 11794, USA

7
8 ²Key Laboratory of Computational Geodynamics of Chinese Academy of Sciences,
9 Graduate University of Chinese Academy of Sciences, Beijing 100049, China

10
11 ³Department of Geosciences, Stony Brook University, Stony Brook, NY 11794, USA

12
13 ⁴Geophysical Laboratory, Carnegie Institution of Washington, Washington DC 20015,
14 USA

15
16 *Corresponding author

17 Email: Baosheng.Li@sunysb.edu

18 Tel: 1-631-632-9642

19 Fax: 1-631-632-8140

20
21 **Keywords:** Brucite, equation of state, X-ray diffraction, infrared spectroscopy

22 **Running title:** Compression and Infrared Study of Brucite

23 **Abstract**

24 Synchrotron X-ray powder diffraction and infrared (IR) spectroscopy studies on
25 natural brucite were conducted up to 31 GPa using diamond anvil cell (DAC) techniques
26 at beamlines X17C and U2A of National Synchrotron Light Source (NSLS). The lattice
27 parameters and unit-cell volumes were refined in $P\bar{3}m1$ space group throughout the
28 experimental pressure range. The anisotropy of lattice compression decreases with
29 pressure due to a more compressible *c* axis and the compression becomes nearly isotropic
30 in the pressure range of 10-25 GPa. The unit cell volumes are fitted to the third-order
31 Birch-Murnaghan equation of state, yielding $K_0 = 39.4(1.3)$ GPa, $K_0' = 8.4(0.4)$ for the
32 bulk modulus and its pressure-derivative, respectively. No phase transition or
33 amorphization was resolved from the X-ray diffraction data up to 29 GPa, however,
34 starting from ~ 4 GPa, a new infrared vibration band (~ 3638 cm^{-1}) 60 cm^{-1} below the OH
35 stretching A_{2u} band of brucite was found to co-exist with the A_{2u} band and its intensity
36 continuously increases with pressure. The new OH stretching band has a more
37 pronounced redshift as a function of pressure (-4.7 $\text{cm}^{-1}/\text{GPa}$) than the A_{2u} band (-0.7
38 $\text{cm}^{-1}/\text{GPa}$). Comparison with first principles calculations suggests that a structural change
39 involving disordered H sublattice is capable of reconciling the observations from X-ray
40 diffraction and infrared spectroscopy studies.

41

42 Introduction

43 Hydrous minerals have long been considered to be the major source for transporting
44 and storing water in the Earth's mantle. Brucite, $\text{Mg}(\text{OH})_2$, is of particular interest for the
45 study of hydrous minerals because of its simple structure in comparison with other
46 hydrous minerals in the Earth's crust and mantle. It can be formed through hydration of
47 olivine in regions where fluid rock interactions are present in the upper mantle.
48 Investigations on the behavior and physical properties of brucite are important for
49 thermodynamic modeling of phase transformations and dehydration processes related to
50 the dynamics at crust and mantle depths (Peacock and Hyndman 1999).

51 At ambient conditions, brucite crystallizes in CdI_2 -type structure with space group
52 $\bar{P}3m1$ (Fig. 1) ($a = 3.1468 \text{ \AA}$, $c = 4.7568 \text{ \AA}$, $c/a = 1.5116$). The MgO_6 layers stack along
53 c axis with an interlayer distance of $\sim 4.71 \text{ \AA}$ while the H atom resides $\sim 0.95 \text{ \AA}$ above
54 oxygen along c axis with three H neighbors from the opposing layer. Much of our
55 understanding about its structural behavior and physical properties at high pressure
56 comes from experimental studies using a variety of techniques, including shock
57 compression (Duffy et al. 1991), X-ray and neutron diffraction (Fei and Mao 1993; Duffy
58 et al. 1995a; Xia et al. 1998; Nagai et al. 2000; Fukui et al. 2003; Parise et al. 1994; Catti
59 et al. 1995; Horita et al. 2010), Raman and infrared spectroscopy (Duffy et al. 1995b,
60 Kruger et al. 1989), and Brillouin scattering measurements (Xia et al. 1998; Jiang et al.
61 2006). Complementary to those from experimental studies, important and insightful
62 results have also been obtained by many researchers using theoretical approaches at
63 conditions within and/or beyond those attained in experiment studies (e.g., Sherman 1991;
64 Raugei et al. 1999; Mookherjee and Stixrude 2006; Jayachandran and Liu 2006;
65 Hermansson et al. 2008; Mitev et al. 2009). In brucite, the atomic interactions between
66 MgO_6 layers along c axis are believed to be weaker than the strong covalent bonds
67 within the layer. This has been demonstrated by data from diffraction studies that the
68 crystallographic c axis is much more compressible than a axis up to $\sim 10 \text{ GPa}$ (e.g., Fei
69 and Mao 1993; Xia et al. 1998; Fukui et al. 2003; Duffy et al. 1995a; Nagai et al. 2000).
70 Above 10 GPa, however, the H atomic positions and the formation of hydrogen bonding
71 become the main dispute, and the results of lattice parameters from different studies also

72 seem to show noticeable divergence with increasing pressure. Neutron diffraction studies
73 on deuterated brucite $\text{Mg}(\text{OD})_2$ (e.g., Parise et al. 1994; Nagai et al. 2000) and molecular
74 dynamic modeling (e.g., Raugei et al. 1999) suggest that there is an increased hydrogen
75 bonding within the hydroxide structure at high pressures when H atoms occupy three
76 off-axial positions (6i site) instead of parallel to *c* axis (2d site). Hydrogen bonding is also
77 suggested in previous Raman and infrared spectroscopy studies based on the observation
78 of new vibration bands at high pressure and the negative pressure dependence of the new
79 bands (Duffy et al. 1995b; Kruger et al. 1989; Shinoda et al. 2002; Horita et al. 2010).
80 However, first principles calculations by Mookherjee and Stixrude (2006) on a $\sqrt{3} \times \sqrt{3} \times 1$
81 superstructure of brucite (space group $\bar{P}3$, H atom at 6g sites) indicate that the formation
82 of interlayer H bond is not a necessity. A more recent molecular dynamics study by Mitev
83 et al. (2009) also argued that the variation of the electrical field when the MgO_6 layers
84 are pressed towards each other at high pressure can be responsible for the negative
85 pressure dependence of the OH vibration bands observed in infrared studies without the
86 formation of H bond.

87 In addition to the ambiguities about crystal structure, the equation of state
88 parameters for brucite, namely, the bulk modulus (*K*) and its pressure derivative (*K'*),
89 from previous studies are still discrepant, ranging from 33 to 68.3 GPa and 8.9 to 4.0,
90 respectively. In comparison, the results calculated using the elastic constants from
91 Brillouin scattering by Xia et al. (1998) and Jiang et al. (2006) yield a value of 36-37 GPa
92 at ambient conditions. It is commonly believed that discrepancy may be introduced by
93 pressure range of experiments, non-hydrostaticity, as well as system errors in different
94 experimental setups. For brucite, structural complications observed at high pressures,
95 such as possible phase transition suggested by Raman study (Duffy et al., 1995b) or
96 compression mechanism change (Nagai et al. 2000), may cast additional uncertainty on
97 the comparability of the data obtained from different pressure ranges.

98 In this paper, new data from high pressure synchrotron X-ray powder diffraction and
99 synchrotron infrared (IR) spectroscopy studies have been acquired on a natural brucite
100 sample. An updated equation of state is derived from X-ray diffraction data under
101 hydrostatic compressions. Attempts have also been made to provide insights in the
102 behavior of H atom at high pressures based on the results of the infrared spectroscopy in

103 conjunction with first principles calculations.

104 **Experimental procedures**

105 Angle-dispersive X-ray powder diffraction experiments were conducted at ambient
106 temperature up to ~29 GPa using a diamond anvil cell (DAC) at beamline X17C of
107 National Synchrotron Light Source (NSLS). Powder sample of natural brucite
108 (GBW03128) with an average chemical composition of MgO (61.43%), CO₂ (8.08%),
109 CaO (2.51%) was used as starting material. The CO₂ and CaO come from dolomite which
110 occurs as a common impurity in natural brucite (see Fig. 2). Brilliant-cut diamond anvils
111 (Type IA) with 250 μm culets were used in the current experiment. A T301 stainless steel
112 gasket was pre-indented from 250 μm to 62 μm in thickness and a hole of 100 μm in
113 diameter was drilled in the center with EDM (Electric Discharge Machine) to serve as the
114 chamber to contain the pressure medium and the sample. A mixture of 16:3:1
115 methanol-ethanol-water was used as pressure medium. Several small ruby crystals were
116 dispersed in the cell and the pressure was obtained from the ruby pressure scale based on
117 the shift of the fluorescent peak (Mao et al. 1986). A beam of monochromatic X-ray
118 (wavelength 0.4066 Å) was focused to a 23 micron (vertical) × 21 micron (horizontal)
119 area using slits and K-B mirrors. Two dimensional diffraction images were collected by
120 using the Rayonix SX165 CCD detector. The scanning time for collecting X-ray
121 diffraction data ranged from 800 to 1200 second based on the intensities of the incident
122 X-ray source. One dimensional diffraction patterns were obtained by an integration of
123 these images over the entire radial coverage using the FIT2D program (Version: V12.077,
124 ESRF). The integrated X-ray diffraction spectra upon increasing pressures are compared
125 in Figure 2 for some selected pressures. Within the diffracting angle of the current setup,
126 four diffraction lines (100), (011), (012) and (110) were recorded at all pressures. The
127 weak non-brucite diffraction peaks could be indexed by dolomite (Fig. 2). These peaks
128 were discarded in the refinement of lattice parameters and unit-cell volumes using the Le
129 Bail method with the software GSAS and the graphical interface EXPGUI (Larson 2004).

130 Synchrotron infrared (IR) spectroscopy experiments on brucite were performed at
131 ambient temperature up to ~31 GPa using a diamond anvil cell at U2A beamline of NSLS.
132 Powder starting material from the same source as that used in the X-ray diffraction

133 experiment was used in IR experiments. A pair of type IIa diamond anvils with a culet
134 size of 300 μm was employed and a pre-indented T301 stainless steel gasket (~ 80 μm
135 thick) with a 100 μm diameter hole was used as the chamber for the sample and the
136 pressure medium. KBr powder was used as a pressure medium together with a small ruby
137 ball loaded into the sample chamber as a pressure standard. The IR spectra were collected
138 in transmission mode by a Bruker FTIR spectrometer with a nitrogen-cooled mid-band
139 MCT (MCT-A) detector. The frequencies of the recorded spectra were from 600 to 8000
140 cm^{-1} with a resolution of 4 cm^{-1} .

141 **Results and discussion**

142 *Linear compression anisotropy*

143 In the refinement of the lattice parameters and unit cell volumes, $P\bar{3}m1$ structure
144 is assumed at all pressures, and the results are listed in Table 1. Broadening of the
145 diffraction lines and decreased diffraction intensities are noticeable at pressures above
146 ~ 14 GPa (Fig. 2), which are believed to be caused by the increased non-hydrostaticity
147 after the solidification of the methanol-ethanol-water pressure medium at ~ 11 GPa (e.g.,
148 Klotz, 2009). As a result, the uncertainties in the refined lattice parameters and unit cell
149 volumes above 14 GPa are about an order of magnitude higher than those below 11 GPa
150 (Table 1). The anisotropic behavior of the lattice compression in brucite is evident when
151 comparing the lattice parameters a and c as a function of pressure. Fitting the observed
152 lattice parameters in the pressure range of 2.0-11.3 GPa to Eulerian finite strain equations
153 (e.g., Meade and Jeanloz, 1990) yields the linear compressibility for both a and c axes, β_a
154 $= 3.4(2) \times 10^{-3} \text{ GPa}^{-1}$ and $\beta_c = 1.8(1) \times 10^{-2} \text{ GPa}^{-1}$, indicating that the compressibility along c
155 axis β_c is about five times of β_a at ambient pressure. This observation is consistent with
156 the anisotropic compression behavior on natural and synthetic brucite samples reported in
157 previous studies. The change of the compression anisotropy with increasing pressure can
158 be inferred from change of the slope in the plot of c/a as a function of pressure based on
159 $\partial(c/a)/\partial P = -(c/a)(\beta_c - \beta_a)$. From ambient pressure to ~ 10 GPa, $\partial(c/a)/\partial P$ changes from \sim
160 -0.017 GPa^{-1} to $\sim -0.003 \text{ GPa}^{-1}$ together with a decrease of c/a from ~ 1.512 to ~ 1.440 , as
161 a result, the difference between β_c and β_a becomes smaller ($\sim 81\%$ reduction in the value

162 of (β_c/β_a) and thus the linear compression anisotropy decreases. Above 10 GPa, c/a
163 becomes less pressure dependent with a slope $\partial(c/a)/\partial P$ close to zero up to ~ 25 GPa,
164 indicating that $\beta_c \cong \beta_a$ and the lattice compression is nearly isotropic. As compared in
165 Figure 3, the c/a values from the current study show a good agreement within 1% with
166 those measured using different techniques except for those from Fei and Mao (1993) with
167 which the agreement is within $\sim 3.5\%$ at ~ 25 GPa and $\sim 6.5\%$ at 29 GPa. Since no pressure
168 medium was used in Fei and Mao (1993), nonhydrostaticity is therefore believed to be
169 responsible for the discrepancy in Figure 3.

170 The characteristics of the c/a ratio and the linear compressibility as a function of
171 pressure are also supported by DFT calculations, although DFT calculations predict a
172 broader pressure range of isotropic compression than those observed in experimental
173 studies (see Fig. 5 in Mookherjee and Stixrude 2006). Both DFT calculations and
174 structural refinement of diffraction data suggest that the initial fast decrease of c/a at low
175 pressures can be attributed to the rapid decrease of the distance between MgO6 layer,
176 presumably because of the weak coulomb and electrostatic forces between these layers.
177 Upon further compression, the interlayer forces become comparable to the intralayer
178 covalent bonds and compressions along a and c axes become comparable, resulting an
179 isotropic compression. It is worth noting that the linear compressibility ratio β_c/β_a
180 calculated using the single crystal elastic constants from Brillouin scattering (Jiang et al.,
181 2006) predicts a value of $\beta_c/\beta_a = 1$ around 20 GPa, which corresponds well to the current
182 observation that c/a ratio becomes pressure independent (i.e., $\beta_c = \beta_a$) at ~ 18 GPa. The
183 c/a value appears to increase with pressure above 25-28 GPa as indicated in the current
184 study and Fei and Mao (1993) as well as DFT calculations, except that DFT calculations
185 suggest a slower increase rate than that observed in previous quasihydrostatic
186 experiments.

187

188 *Equation of state*

189 The unit cell volumes obtained from the current study are plotted as a function of
190 pressure in Figure 4. Isothermal bulk modulus (K_0) and its pressure derivative (K_0') are
191 constrained by fitting these data to the third-order Birch-Murnaghan equation of state,

$$P = \frac{3}{2} K_0 \left[\left(\frac{V_0}{V} \right)^{\frac{7}{3}} - \left(\frac{V_0}{V} \right)^{\frac{5}{3}} \right] \cdot \left\{ 1 + \frac{3}{4} (K_0' - 4) \cdot \left[\left(\frac{V_0}{V} \right)^{\frac{2}{3}} - 1 \right] \right\}$$

192
193 where V_0 is the unit cell volume, and the subscript “0” refers to ambient pressure. An
194 unweighted fit to the data in entire pressure range yields $K_0 = 37.0(1.3)$ GPa, $K_0' = 10.6$
195 (0.4) with V_0 fixed at the observed value 40.794 \AA^3 . Considering that the data at pressures
196 higher than ~ 11 GPa may be affected by the present of deviatoric stresses as well as a
197 possibility that the compression mechanism changes from interlayer distance shortening
198 to isotropic compression as suggested by Nagai et al. (2000), we therefore performed a fit
199 using the data only up to ~ 11 GPa where the pressure medium is known to be hydrostatic
200 (e.g., Klotz 2009). The results from the latter fit, $K_0 = 39.4(1.3)$ GPa, $K_0' = 8.4(0.4)$, and
201 $V_0 = 40.909 \text{ \AA}^3$, are believed to be a more reliable constraint for the bulk modulus and its
202 pressure derivative at ambient pressure, and are therefore used as the representative
203 values from the current study (Table 2). Following the analysis of Angel (2000), the
204 negative correlation between K_0 and K_0' in the least square fit is illustrated by the 95%
205 confidence ellipse of the two parameters (Fig. 5).

206 As shown in Table 2, the values of K_0 and K_0' for brucite from previous studies are
207 largely discrepant, ranging from 33 to 68.3 GPa and 8.9 to 4.0, respectively. The values
208 from Brillouin scattering measurements by Xia et al. (1998) and Jiang et al. (2006),
209 however, give a fairly consistent result of 36-37 GPa for the bulk modulus at ambient
210 pressure. Unlike equation of state fit which must incorporate measurements of pressure
211 and volume at high pressures, Brillouin scattering provides direct measurements of
212 acoustic velocities and therefore the elastic constants at each pressure. The good
213 agreement of K_0 and K_0' from the current equation of state fit with the results of $K_0 = 35.8$
214 GPa and $K_0' = 8.9$ derived from Brillouin scattering data of Jiang et al. (2006) further
215 validates the current determinations. When compared to previous compression studies,
216 reasonably good agreement can be found with those from measurements on $\text{Mg}(\text{OH})_2$
217 brucite (Horita et al. 2010; Fukui et al. 2003; Catti et al. 1995; Xia et al. 1998) as well as
218 on deuterated brucite $\text{Mg}(\text{OD})_2$ (Nagai et al., 2000). A discontinuity has been suggested
219 by Fei and Mao (1993) in the unit cell volume as a function of pressure around 8-11 GPa,
220 but this has not been observed in other studies. Nevertheless, if the data in the pressure

221 range up to 11 GPa from Fei and Mao (1993) are used in equation of state fit, a bulk
222 modulus of 42.8 GPa can be obtained (with K_0' and V_0 fixed at the values of the current
223 study), which is in much better agreement with those compared in Table 2. Thus, the
224 primary sources for the observed discrepancy include (1) trade-off between K_0 and K_0'
225 when fitting datasets obtained from different pressure ranges, and (2) differences in stress
226 states in different experiments (see also Horita et al. 2010, Jiang et al. 2006). While these
227 trade-off between K_0 and K_0' can be investigated retroactively using the published
228 volumes, the assessment and correction for the effects of stress on the data listed in Table
229 2, however, are difficult due to the lack of quantitative stress information from these
230 studies.

231

232 OH Vibration and H Position

233 Brucite ($P\bar{3}m1$) has two internal OH vibrational modes at ambient conditions, an
234 infrared active OH stretching mode (A_{2u} mode) at $\sim 3697\text{ cm}^{-1}$ and a Raman active A_{1g}
235 mode at $\sim 3650\text{ cm}^{-1}$. Previously, Kruger et al. (1989) reported that a new infrared band
236 was observed at pressure as low as zero pressure, with its intensity gradually increased to
237 30% of the intensity of A_{2u} mode at 29 GPa. Both the A_{2u} and the new bands were found
238 to exhibit redshift in frequency (i.e., negative pressure dependence). They attributed the
239 new OH stretching band to a transition from the first excited infrared state to its first
240 overtone ($A_{2u} \times A_{2u}$). However, in the reports of Shinoda and Aikawa (1998) and
241 Shinoda et al. (2002), a new peak $\sim 50\text{ cm}^{-1}$ below the fundamental infrared A_{2u} peak was
242 observed only at pressures over ~ 3 GPa, and it was assigned to a new OH dipole due to
243 the formation of new proton site at high pressure.

244 Our infrared results yielded 3698 cm^{-1} for the frequency of the A_{2u} mode at ambient
245 conditions, which is very consistent with the values reported in previous studies. At ~ 4
246 GPa, a new vibrational peak started to appear at $\sim 3638\text{ cm}^{-1}$ and its intensity increases
247 with pressure (Fig. 5). The pressures at which the new peak was observed agrees well
248 with the pressure range where new Raman and IR peaks were observed in previous
249 studies (e.g., Duffy et al. 1995b; Shinoda and Aikawa 1998; Shinoda et al. 2002). The
250 current A_{2u} band and the new mode exhibit redshifts as a function of pressure with a slope

251 of $-0.7 \text{ cm}^{-1}/\text{GPa}$ and $-4.7 \text{ cm}^{-1} /\text{GPa}$, respectively. These results compare well with
252 previously reported values of $-0.6 \text{ cm}^{-1}/\text{GPa}$ and $-3.7 \text{ cm}^{-1}/\text{GPa}$ obtained by Kruger et al.
253 (1989), as well as $-0.25 \text{ cm}^{-1}/\text{GPa}$ and $-5.0 \text{ cm}^{-1}/\text{GPa}$ by Shinoda et al. (2002) (Fig. 6).
254 The redshifts of both the fundamental and the new peak are completely reversible along
255 decompression without noticeable hysteresis. Within the pressure range where the new
256 infrared peak co-exists with the fundamental A_{2u} mode, no phase transition in brucite can
257 be resolved in the X-ray diffraction patterns, except for a change in the linear
258 compression anisotropy as indicated in the c/a as a function of pressure in Figure 3.
259 These results appear to agree with previous suggestions that the structural variation of
260 brucite at pressure is primarily associated with the rearrangement of H atoms while the
261 MgO6 sublattice remains unaffected.

262 As inferred in previous studies, H atoms in $\text{Ca}(\text{OH})_2$ undergo an order-disorder
263 transition marked by an abrupt increase in the width of the A_{2u} band at $\sim 11\text{-}12\text{GPa}$, and
264 the disordering of H atoms destabilizes the CaO6 sublattice and leads to the
265 amorphization of $\text{Ca}(\text{OH})_2$ (e.g., Desgranges et al. 1996; Nagai et al. 2000). In another
266 brucite-type metal hydroxide, $\text{Co}(\text{OH})_2$, whose metal cation radius is slightly smaller than
267 Ca, only partially disordered H sublattice was inferred from Raman and infrared data at
268 30 GPa with clear evidence from X-ray diffraction indicating that long range order of
269 CoO6 sublattice was still preserved. By comparison, the width of the A_{2u} band for
270 $\text{Mg}(\text{OH})_2$ from the current study shows a linear increase with pressure up to $\sim 30\text{ GPa}$,
271 consistent with previous observations by Kruger et al. (1989) and Nguyen et al. (1997). It
272 has been suggested that brucite-type hydroxides with large metal cation mirror the atomic
273 interactions and therefore the structural behavior of those with smaller metal cation at
274 higher pressures. Mg has a smaller cationic radius in comparison with Ca and Co, the
275 observation of new band and the lack of abrupt FWHM increase in the fundamental A_{2u}
276 band and the new OH band appear to indicate a partial disorder and the possibility of
277 additional H sites.

278 Quantitative determination of the atomic positions H for brucite under high pressure,
279 however, remains as a challenging task. Neutron diffraction studies on deuterated brucite
280 $\text{Mg}(\text{OD})_2$ (Parise et al., 1994) suggest that at non-ambient pressures D atom is displaced
281 from its axial position (2d) to three off-axis positions (6i) with equal probability of

282 occupancy, resulting from either random static disorder or anharmonic thermal vibration.
283 The OD distance refined with D atoms at $6i$ sites shows nearly no change from 0 to 2
284 GPa followed by a continuous increase from ~ 0.95 Å to 1.02 Å to 9.3 GPa. A subsequent
285 neutron diffraction study (Catti et al., 1995) on normal brucite $\text{Mg}(\text{OH})_2$, however, finds
286 that H ordered model (H in 2d site) is favored at low pressures (0-7.8 GPa) while both the
287 ordered and disordered (H in $6i$ site) models fit the data at 10.9 GPa equally well. The
288 refinement results revealed a continuous decrease in OH distance from 0.958 Å to 0.915
289 Å with H at 2d site ($P < 10$ GPa) and $6i$ site ($P > 10$ GPa). Molecular dynamic simulation
290 (Raugei et al. 1999) indicates that vigorous anharmonic motions of H atoms in $\text{Mg}(\text{OH})_2$
291 and $\text{Ca}(\text{OH})_2$ can displace H atoms from the threefold axis and result in disordering of H
292 sublattice at high pressures. In addition, the pressure induced redshifts of A_{2u} modes
293 observed in previous experiments of Kruger et al. (1989) can be reproduced with such a
294 disordered H model. Mookherjee and Stixrude (2006) conducted first principles
295 calculations on brucite using a $\sqrt{3} \times \sqrt{3} \times 1$ super cell of brucite, and found that this model
296 structure with H occupying 6g site at $\sim 7^\circ$ off from threefold axis is energetically favored
297 at high pressure.

298 We conducted *ab initio* calculations for both $P\bar{3}m1$ and $P\bar{3}$ structures using
299 density functional theory (DFT) within the GGA framework as implemented in CASTEP
300 (Clark et al., 2005). An energy cutoff of 800 eV for the plane wave basis set and k point
301 sampling of $9 \times 9 \times 5$ ($P\bar{3}m1$) and $7 \times 7 \times 7$ ($P\bar{3}$) were used to ensure an energy convergence
302 of 1×10^{-6} eV/atom and 0.02 GPa in pressure. The OH distances in these two structures are
303 found to have very limited sensitivity to pressure. In $P\bar{3}m1$, the OH distance shows a
304 negligible increase from 0.9753 Å at ambient pressure to 0.9757 Å at ~ 5 GPa (0.04%)
305 followed by a small decrease to 0.9736 Å at 30 GPa. By comparison, the OH distance in
306 $P\bar{3}$ structure ($\sqrt{3} \times \sqrt{3} \times 1$) slowly increases from 0.9756 at zero pressures to 0.9773 Å at 5
307 GPa and then to 0.9830 Å at 30 GPa. In spite of the minor differences in OH distance and
308 orientation between $P\bar{3}$ and the $P\bar{3}m1$ structures, the MgO_6 sublattices in both
309 structures remain indistinguishable at high pressures. Attempt to distinguish the structure
310 of brucite based on the OH distances from previous neutron diffraction studies on

311 Mg(OH)₂ and Mg(OD)₂, however, seems to be difficult due to the discrepancies between
312 the results from these two studies. Comparisons of structural changes and energetics
313 between $\bar{P}3m1$ and $\bar{P}3$ structures in a wide pressure range have been given in detail
314 in the DFT study of Mookherjee and Stixrude (2006), and will not be repeated here.
315 Instead, we will provide supplementary vibration spectroscopy data from DFT
316 calculations to compare with those from high pressure experiments.

317 Infrared spectra for both $\bar{P}3m1$ and $\bar{P}3$ structures at high pressures are calculated
318 using a linear response approach with norm-conserving potentials as implemented in
319 software CASTEP. It has been demonstrated that the harmonic OH stretching frequencies
320 derived within GGA show good agreement with the experimental frequencies resulting
321 from a cancellation of the overestimation of bond length and the underestimation of
322 harmonic frequencies associated with GGA approximation in DFT calculations (Balan et
323 al., 2007). The fundamental frequency of the A_{2u} mode for $\bar{P}3m1$ from the current
324 calculation is 3651 cm⁻¹, which is within 1.5% agreement with the experimental results
325 from the current as well as previous studies (3698-3700 cm⁻¹). The calculated Raman
326 active OH modes A_{1g} (3612 cm⁻¹) is within ~1% of the single crystal data reported by
327 Duffy et al. (1995a) (3652 cm⁻¹). With increasing pressure from 0 to 10 GPa, the A_{2u}
328 mode displays a slight decrease in frequency with a pressure dependence of $dv/dP \sim -0.7$
329 cm⁻¹/GPa, which is consistent with the experimentally observed value (Fig. 6). Above 10
330 GPa, the OH vibration frequencies increase slightly with pressure with a rate of ~1.0
331 cm⁻¹/GPa. No pressure induced new vibration band was observed when the H positions
332 maintain parallel to the c-axis at the 2d positions in $\bar{P}3m1$ structure. In $\bar{P}3$ structure
333 with H atom inclined at ~7.4° from the threefold axis at zero pressure, an OH stretching
334 vibration frequency of 3643 cm⁻¹ is observed which is slightly lower than the A_{2u} mode in
335 the $\bar{P}3m1$ structure. With increasing pressure, the OH stretching vibration frequency in
336 $\bar{P}3$ decreases at a rate of -5.0 cm⁻¹/GPa, which is in excellent agreement with the
337 pressure dependence of the new band (-4.7 cm⁻¹/GPa) observed in our experiment (Fig. 6).
338 Interestingly, the new Raman modes observed in previous study by Duffy et al. (1995b)

339 can be found in the Raman active modes for $\bar{P}3$ structure. In comparison, previous
340 calculation on $\text{Mg}(\text{OH})_2$ (Mitev et al. 2009) predicts that the redshift of A_{2u} mode under
341 an isotope isolated configuration has a slope of $dv/dP = -4 \text{ cm}^{-1}/\text{GPa}$ with H parallel to
342 c -axis (H at 2d site) and a much larger pressure dependence ($-11 \text{ cm}^{-1}/\text{GPa}$) for OH
343 stretching band when H atoms are displaced from the c axis (H at 6g site, $\bar{P}3$).

344 Qualitatively, the current findings agree with previous suggestions that H atoms
345 occupying off-axis positions are capable of producing the new OH stretching band
346 observed in high pressure infrared data (e.g., Raugei et al. 1999; Mookherjee and
347 Stixrude 2006; Mitev et al. 2009; Jochym et al. 2010). Quantitative comparison of dv/dP
348 between current calculations and experimental infrared data seems to suggest that the
349 co-existence of the original A_{2u} band and the new OH stretching band observed in
350 infrared experiments requires H atoms to take occupancies at both axial and off-axis
351 positions. Possible scenarios include the development of off axis H atoms in a locally
352 ordered form (e.g., a $\bar{P}3$ -like structure) as a separate phase/cluster/domains as driven by
353 the lower enthalpy, or a structure involving intermixed axial and off-axial H atoms which
354 maintains a long range order within the crystal but with locally disordered H sites. If it is
355 the former, the interaction of the H sublattices from each phase is insignificant and the
356 characteristics of each structure are preserved in experimental measurements. Evidences
357 supporting this model include weak neutron diffraction lines besides those from $\bar{P}3m1$
358 structure (e.g., Horita et al. 2010), volume discontinuities at 8-11 GPa (see Fei and Mao
359 1993), new Raman (Duffy et al. 1995b) and infrared data as shown above, as well as
360 lower enthalpy of $\bar{P}3$ structure in DFT results. Along this line, the increase of the
361 FWHM for both OH stretching bands (Fig. 5) may suggest that the disordering of H in
362 the two phases continues to increase with pressure, when the two OH vibrations bands
363 merge into a broad band at higher pressures, and it may result in full disorder. It is
364 interesting to note that a recent X-ray diffraction study suggests that the behavior of
365 $\text{Ca}(\text{OH})_2$ at high pressure appears to follow this pathway, in which a crystal-crystal phase
366 transition was indeed observed prior to its amorphization (Iizuka et al. 2011).

367 Alternatively, a structure model with intermixed (locally disordered) H atoms and

368 long-range order is equally valid. Previously, infrared studies with polarized and
369 unpolarized sources by Shinoda et al. (2002) suggested that brucite at high pressures
370 undergoes a proton state transition from one proton site to two proton state in which the
371 H bonds of trifurcated and bent types are responsible for the original and pressure
372 induced new OH bands. A recent molecular dynamics study also indicated that H atoms
373 could be decoupled from brucite lattice into “lock-in” off-axis positions. We constructed
374 a 3 x 3 x 1 supercell of brucite in $\bar{P}3$ structure (see Fig. 5 of Mitev et al. 2009) and
375 performed structure optimization using DFT within GGA. We found that if the initial H
376 atoms are at the off-axis positions, structure optimization results in a lower enthalpy
377 structure with two distinct groups of OH distances and off-axis angles. This implies that
378 when the distance between MgO6 layers decreases with increasing pressure, if some H
379 atoms are displaced into off axis positions due to either anharmonic motions or
380 electrostatic forces, the resulting structure with locally disordered H atoms can be
381 energetically favored. This is also observed in a 2 x 2 x 1 supercell in $\bar{P}3$ (20 atoms/cell,
382 H at 2d and 6g sites, Mg: 1a and 3e sites), in which the co-existing two H sites resemble
383 those in $\bar{P}3$ (H off axis) and $\bar{P}3m1$ (H parallel to axis) structures. At 20 GPa, the
384 optimized 2 x 2 x 1 supercell has an enthalpy ~ 0.005 eV/atom lower than $\bar{P}3m1$ (H at
385 2d site) but 0.003 eV/atom higher than the $\bar{P}3$ (H atoms all at 6g sites). We calculated
386 the infrared spectra for the 2 x 2 x 1 supercell, and two separate OH stretching bands
387 were indeed observed. However, the redshifts of the OH stretching bands from our DFT
388 calculations yielded results similar to those reported for isotope-isolated OH frequencies
389 (Mitev et al. 2009), which are much larger than those observed in the infrared
390 experiments.

391

392 **Concluding Remarks**

393 We have conducted synchrotron X-ray powder diffraction, infrared spectroscopy,
394 and DFT studies to investigate the structural behavior under compression, equation of
395 state and vibrational properties of brucite. Refinements of the lattice parameters and

396 unit-cell volumes were performed in $\bar{P}3m1$ space group throughout the experimental
397 pressure range. The current results suggest that under pressures equivalent to the Earth's
398 upper mantle and transition zone, the compressibility of brucite along c and a axes
399 gradually changes from anisotropic to isotropic. The unit cell volumes under hydrostatic
400 pressures are fitted to the third-order Birch-Murnaghan equation of state, yielding $K_0 =$
401 $39.4(1.3)$ GPa, $K_0' = 8.4(0.4)$ for the bulk modulus and its pressure-derivative,
402 respectively. These results are in good agreement with previous compression studies at
403 similar pressure conditions. Discrepancies in literature values may arise from differences
404 in pressure range, non-hydrostaticity on the sample, and the possibility that brucite
405 experiences a compression mechanism change or phase transition at high pressures.

406 While the new OH vibration band observed in infrared data is in general agreement
407 with trifurcated H atoms suggested by Neutron diffraction and molecular dynamics, a
408 comparison of the infrared spectra from DFT calculations with those from experiments
409 indicates that the dv/dP of the original OH band is similar to the A_{2u} band in $\bar{P}3m1$ with
410 H atoms at 2d site, while the dv/dP of the new OH band is nearly identical to the OH
411 stretching band in $\bar{P}3$ with H at off-axis positions (6g site). We investigated two
412 scenarios at high pressure which only involve the change of H atoms in the lattice, the
413 first is that brucite slowly transforms into a new phase with lower enthalpy and off-axis H
414 positions (e.g., a $\bar{P}3$ like structure) so that within crystal scale H atoms appear to be
415 disordered but ordered in each phase; the second is that both axial and off-axial OH
416 bonds closely intermixed to form locally disordered H atoms in the new structure with
417 long range order within the crystal. While direct experimental evidences to discern these
418 two candidates are still lacking, a comparison with existing experimental data, especially
419 the pressure dependence of the redshifts of OH stretching bands, seems to favor the
420 development of off axial H positions in a separate phase, although the test for the
421 intermixed OH bonds might suffer from uncertainties caused by the small size of
422 supercell investigated in this study. In either cases, the increased FWHM of the OH
423 stretching bands may be interpreted as the increased disordering of H atoms at high
424 pressure, which may ultimately lead to a fully disorder H sublattice and possibly

425 amorphization following the pathways suggested in Ca(OH)₂ (Iizuka et al. 2011).

426 **Acknowledgments**

427 We would like to thank the editor and Drs. Monika Koch-Müller and Mainak
428 Mookherjee for their constructive reviews to improve the manuscripts. This research was
429 partially supported by COMPRES, the Consortium for Materials Properties Research in
430 Earth Sciences under NSF Cooperative Agreement EAR 1043050. Use of the National
431 Synchrotron Light Source, Brookhaven National Laboratory, was supported by the U.S.
432 Department of Energy, Office of Science, Office of Basic Energy Sciences, under
433 Contract No. DE-AC02-98CH10886. MM thanks for the financial support provided by
434 National Natural Science Foundation of China (40774047) and Knowledge Innovation
435 Project of Chinese Academy of Science (KZCX2-EW-QN602). BL acknowledges
436 financial support from DOE/NNSA (DE-FG5209NA29458) and NSF (EAR1045630).

437

438 **References**

- 439 Angel, R. J. (2000) Equations of state. in “High-Pressure and High-Temperature Crystal
440 Chemistry”, R.M. Hazen & R.T. Downs, eds. MSA Rev. Mineral. Geochem. 41,
441 35–60.
- 442 Balan, E., Lazzeri, M., Delattre, S., Me’heut, M., Refson, K., and Winkler, B., (2007)
443 Anharmonicity of inner-OH stretching modes in hydrous phyllosilicates: assessment
444 from first-principles frozen-phonon calculations, *Physics and Chemistry of Minerals*,
445 34, 621–625.
- 446 Catti, M., Ferraris, G., Hull, S., and Pavese, A., (1995) Static compression and H-disorder
447 in Brucite, Mg(OH)₂, to 11 GPa—a powder neutron diffraction study. *Physics and*
448 *Chemistry of Minerals*, 22, 200–206.
- 449 Clark, S.J., Segall, M.D., Pickard, C.J., Hasnip, P.J., Probert, M.J., Refson K., and Payne,
450 M.C. (2005) First principles methods using CASTEP, *Zeitschrift fuer*
451 *Kristallographie*, 220, 567–570.
- 452 Desgranges, L., Calvarin, G. and Chevrier, G., (1996) Interlayer interactions in M(OH)₂:
453 a neutron diffraction study of Mg(OH)₂, *Acta Crystallographica*, B52, 82–86.

- 454 Duffy, T.S. and Ahrens, T.J. (1991) The shock-wave equation of state of brucite $\text{Mg}(\text{OH})_2$.
455 Journal of Geophysical Research, 96B, 14319–14330.
- 456 Duffy, T.S., Shu, J.F., Mao, H.K., and Hemley, R.J. (1995a) Single-crystal
457 X-ray diffraction of brucite to 14 GPa. Physics and Chemistry of Minerals, 22,
458 277–281.
- 459 Duffy, T.S., Maede, C., Fei, Y., Mao, H.K., and Hemley, R.J. (1995b) High pressure
460 phase transition in brucite, $\text{Mg}(\text{OH})_2$. American Mineralogist, 80, 222–230.
- 461 Fei, Y.W. and Mao, H.K., (1993) Static Compression of $\text{Mg}(\text{OH})_2$ to 78-GPa at
462 High-Temperature and Constraints on the Equation of State of Fluid H_2O . Journal of
463 Geophysical Research, 98, 11875–11884.
- 464 Fukui, H., Ohtaka, O., Suzuki, T., and Funakoshi, K., (2003) Thermal expansion of
465 $\text{Mg}(\text{OH})_2$ brucite under high pressure and pressure dependence of entropy. Physics
466 and Chemistry of Minerals, 30, 511–516.
- 467 Hermansson, K., Gajewski, G., and Mitev, P.D., (2008) Pressure-induced OH frequency
468 downshift in brucite: frequency-distance and frequency-field correlations. Journal of
469 Physics: Conference Series, 117, 1–8.
- 470 Horita, J., Santos, A.M., Tulk, C.A., Chakoumakos, B.C., and Polyakov, V.B., (2010)
471 High-pressure neutron diffraction study on H-D isotope effects in brucite. Physics
472 and Chemistry of Minerals, 37, 741–749.
- 473 Iizuka, R., Kagi, H., Komatsu, K., Ushijima, D., Nakano, S., Sano-Furukawa, A., Nagai,
474 T., and Yagi, T., (2011), Pressure responses of portlandite and H–D isotope effects
475 on pressure-induced phase transitions, Physics and Chemistry of Minerals, 38,
476 777–785.
- 477 Jochym, P.T., Oleś, A.M., Parlinski, K., Łażewski, J., Piekarczyk, P., and Sternik, M., (2010)
478 Structure and elastic properties of $\text{Mg}(\text{OH})_2$ from density functional theory, Journal
479 of Physics: Conference Series, 22, 445403.
- 480 Jayachandran, K.P. and Liu, L.G. (2006) High pressure elasticity and phase
481 transformation in brucite, $\text{Mg}(\text{OH})_2$. Physics and Chemistry of Minerals, 33,
482 484–489.
- 483 Jiang, F.M., Speziale, S., and Duffy, T.S., (2006) Single-crystal elasticity of brucite,
484 $\text{Mg}(\text{OH})_2$, to 15 GPa by Brillouin scattering. American Mineralogist, 91,

- 485 1893–1900.
- 486 Klotz, S., Chervin, J-C, Munsch, P., and Marchand, G.L., (2009) Hydrostatic limits of 11
487 pressure transmitting media. *Journal of Physics D: Applied Physics*, 42, 075413.
- 488 Kruger, M.B., Williams, Q., and Jeanloz, R., (1989) Vibrational spectra of Mg(OH)₂ and
489 Ca(OH)₂ under pressure. *The Journal of Chemical Physics*, 91, 5910–5915.
- 490 Larson, A.C. and Von Dreele, R.B., (2004) General Structure Analysis System (GSAS),
491 Los Alamos National Laboratory Report LAUR, 86–748.
- 492 Mao, H.K., Xu, J., and Bell, P.M., (1986) Calibration of the ruby pressure gauge to 800
493 kbar under quasi-hydrostatic conditions. *Journal of Geophysical Research*, 91,
494 4673–4676.
- 495 Meade, C. and Jeanloz, R., (1990) Static compression of Ca(OH)₂ at room-temperature
496 observations of amorphization and equation of state measurements to 10.7 GPa.
497 *Geophysical Research Letters*, 17: 1157–1160.
- 498 Mitev, P.D., Gajewski, G., and Hermansson, K., (2009) Anharmonic OH vibrations in
499 brucite: small pressure-induced redshift in the range 0–22 GPa. *American*
500 *Mineralogist*, 94, 1687–1697.
- 501 Mookherjee, M. and Stixrude, L., (2006) High-pressure proton disorder in brucite.
502 *American Mineralogist*, 91, 127–134.
- 503 Nagai, T., Hattori, T., and Yamanaka, T., (2000) Compression mechanism of brucite: An
504 investigation by structural refinement under pressure. *American Mineralogist*, 85,
505 760–764.
- 506 Nguyen, Jeffrey H., Kruger, Michael B., and Raymond, Jeanloz, (1997) Evidence for
507 “Partial” (Sublattice) Amorphization in Co(OH)₂, *Physical Review Letters*, 78,
508 1936–1939.
- 509 Parise, J.B., Leinenweber, K., Weidner, D.J., Tan, K., and Von Dreele, R.B. (1994)
510 Pressure-induced H bonding; neutron diffraction study of brucite, Mg(OD)₂.
511 *American Mineralogist*, 79, 193–196.
- 512 Peacock, S.M. and Hyndman, R.D. (1999) Hydrous minerals in the mantle wedge and the
513 maximum depth of subduction thrust earthquakes. *Geophysical Research Letters*, 26,
514 2517–2520.
- 515 Raugé, S., Silvestrelli, P.L., and Parrinello, M., (1999) Pressure-induced frustration and

- 516 disorder in $\text{Mg}(\text{OH})_2$ and $\text{Ca}(\text{OH})_2$. Physical Review Letters, 83, 2222–2225.
- 517 Sherman, D.M., (1991) Hartree–Fock band-structure, equation of state, and
518 pressure-induced hydrogen-bonding in brucite, $\text{Mg}(\text{OH})_2$. American Mineralogist,
519 76, 1769–1772.
- 520 Shinoda, K. and Aikawa, N., (1998) Interlayer proton transfer in brucite under pressure
521 by polarized IR spectroscopy to 5.3 GPa. Physics and Chemistry of Minerals, 25,
522 197–202.
- 523 Shinoda, K., Yamakata, M., Nanba, T., Kimura, H., Moriwaki, T., Kondo, Y., Kawamoto,
524 T., Niimi, N., Miyoshi, N., and Aikawa, N., (2002) High pressure phase transition
525 and behavior of protons in brucite $\text{Mg}(\text{OH})_2$: a high-pressure-temperature study
526 using IR synchrotron radiation. Physics and Chemistry of Minerals, 29, 396–402.
- 527 Xia, X., Weidner, D.J., and Zhao, H. (1998) Equation of state of brucite: Singlecrystal
528 Brillouin spectroscopy study and polycrystalline pressure-volume-temperature
529 measurement. American Mineralogist, 83, 68–74.

530

531 **Figure Captions:**

532 Fig. 1. Crystal structure of brucite ($P\bar{3}m1$) viewed along c axis (a) and a axis (b). H
533 atoms are shown as light colored balls, and the red balls are oxygen and orange balls are
534 Mg atoms.

535

536 Fig. 2. X-ray diffraction patterns of brucite at six selected pressures during compression
537 at room temperature (“D” denotes peaks from dolomite).

538

539 Fig. 3. Comparison of c/a from this study with those from previous experimental studies.

540

541 Fig. 4. (a) Comparison of V/V_0 from the current study with previous experimental results.
542 (b) Confidence ellipse of $K_0 - K_0'$ from the current least square fit to the data within
543 hydrostatic pressure limit (0–11.3 GPa). The symbols are the $K_0 - K_0'$ values from
544 previous experimental studies listed in Table 2 (except Fei and Mao 1993). H: Horita et al.
545 (2010); J: Jiang et al. (2006); F: Fukui et al. (2003); N: Nagai et al. (2000); X: Xia et al.
546 (1998); C: Catti et al. (1995); D: Duffy et al. (1995).

547

548 Fig. 5. Infrared spectroscopy data of brucite at high pressure and ambient temperature
549 along compression (a), (b), and decompression (c).

550

551 Fig. 6. Comparison of pressure-induced redshifts of the OH vibration frequencies from
552 experimental and theoretical studies.

553

Table 1. Refined lattice parameters and unit-cell volumes at ambient temperature.

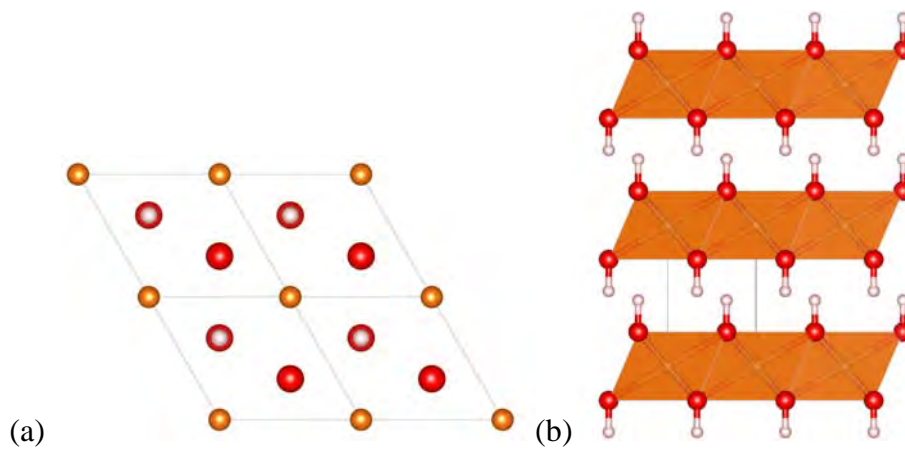
P (GPa)	a (Å)	c (Å)	Volume (Å³)
0	3.1468(9)	4.7568(12)	40.794(19)
1.58	3.121(4)	4.6897(12)	39.56(7)
2.30	3.1241(4)	4.6188(16)	39.039(16)
3.03	3.1159(4)	4.5867(17)	38.566(16)
3.92	3.1056(5)	4.5504(18)	38.008(17)
4.91	3.0960(6)	4.5187(23)	37.510(22)
5.91	3.0863(6)	4.4896(23)	37.035(22)
7.01	3.0748(6)	4.4591(23)	36.509(22)
8.28	3.0631(7)	4.4279(25)	35.978(23)
9.55	3.0528(8)	4.4041(31)	35.545(28)
11.30	3.0435(8)	4.3781(28)	35.121(26)
12.47	3.0367(10)	4.354(4)	34.769(32)
14.18	3.0282(13)	4.334(5)	34.42(4)
16.81	3.0144(19)	4.300(7)	33.84(6)
18.26	3.0037(15)	4.293(5)	33.54(5)
19.78	3.0019(19)	4.250(7)	33.17(6)
20.70	2.9865(27)	4.280(10)	33.06(9)
22.28	2.9725(26)	4.274(10)	32.71(9)
24.90	2.9642(28)	4.244(11)	32.29(9)
26.60	2.9436(30)	4.266(12)	32.01(10)
28.92	2.9224(14)	4.317(4)	31.93(4)

Table 2. Experimental and calculated bulk modulus (K_0) and its pressure derivative (K_0') from this study and the literature

V_0 (Å ³)	K_0 (GPa)	K_0'	Method	Pressure Medium	Source
Experimental					
40.909	39.4(1.3)	8.4 (0.4)	Powder X-ray	Methanol-ethanol-	This study ¹
40.794	37.0 (1.3)	10.6 (0.4)	Powder X-ray	water (16:3:1)	This study ²
41.1752	39.0 (2.8)	11.1 (2.0)	Powder neutron	Fluorinert	Horita et al. 2010
	35.8 (0.9)	8.9 (0.4)	Brillouin scattering	Methanol-ethanol (4:1)	Jiang et al. 2006
40.930	41.8 (1.3)	6.6 (0.3)	Powder X-ray	Magnesium oxide	Fukui et al. 2003
40.746	44 (1)	6.7 (fixed)	Powder X-ray	Methanol-ethanol (4:1)	Nagai et al. 2000
40.8	39.6 (1.4)	6.7 (0.7)	Powder X-ray	Boron nitride	Xia et al. 1998
40.986	39 (1)	7.6 (0.7)	Powder neutron	NaCl	Catti et al. 1995
40.851	42 (2)	5.7 (0.5)	Single-crystal X-ray	None or Ne	Duffy et al. 1995
40.878	54.3 (2)	4.7 (0.2)	Powder X-ray	None	Fei and Mao 1993
Theory					
41.699	39.7	6.75	DFT (GGA)		Mitev et al. 2009
42.991	33		B3LYP		Hermansson et al. 2008
36.7	65	6.0	DFT (LDA)		Mookherjee and Stixrude 2006
41.7	43	5.7	DFT (GGA)		
40.86	68.3	4.0	Hartree-Fock		Sherman 1991

¹: Fit without weight, hydrostatic pressures, 0-11.3 GPa,

²: Fit without weight, all data, 0-28.9 GPa.



(a)
Figure 1.

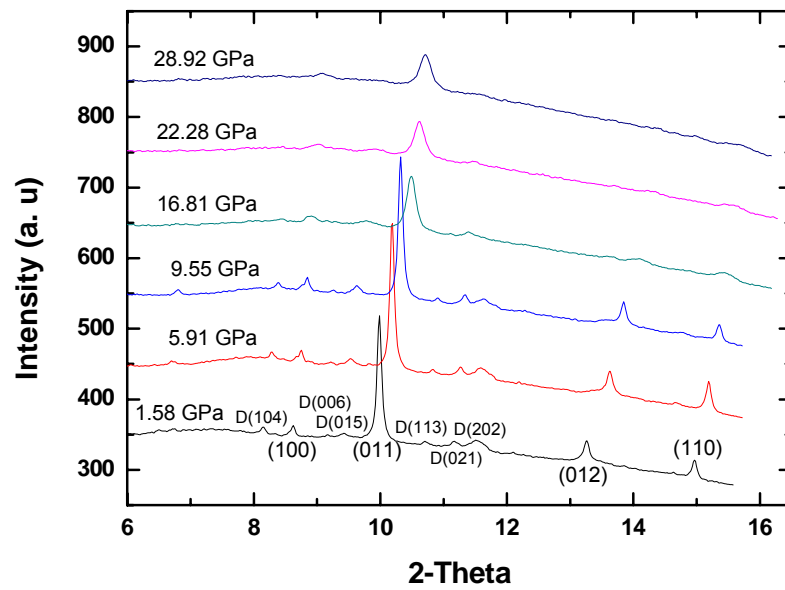


Figure 2.

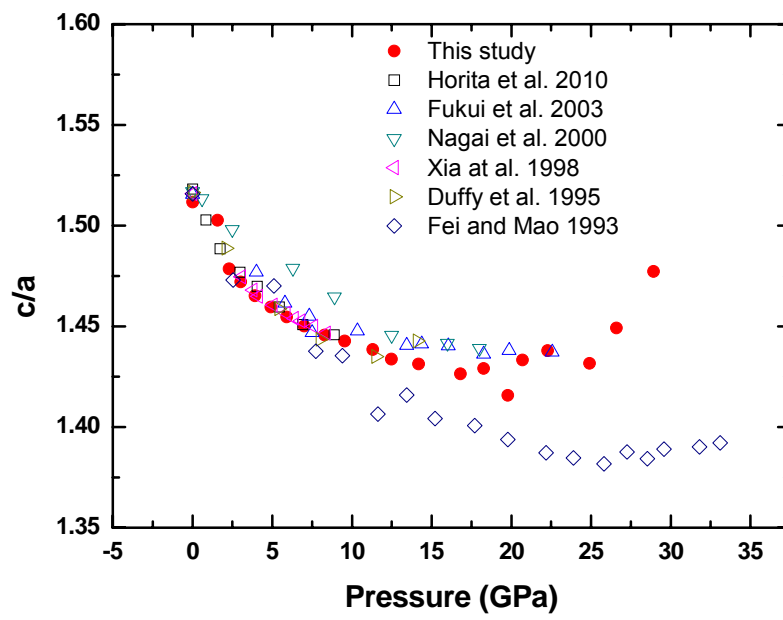
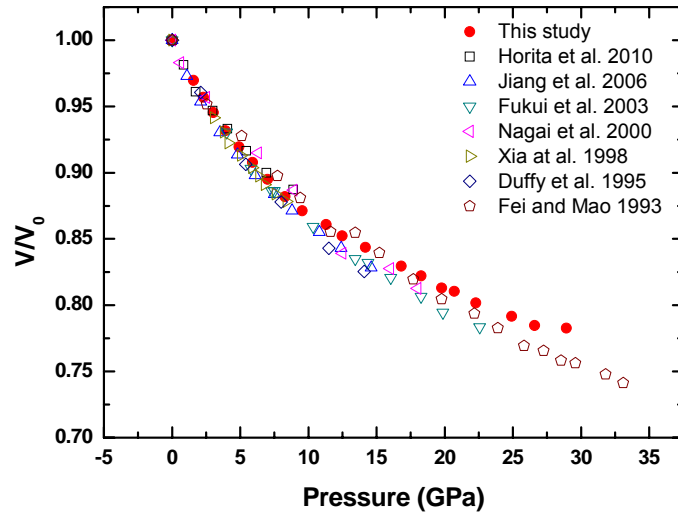
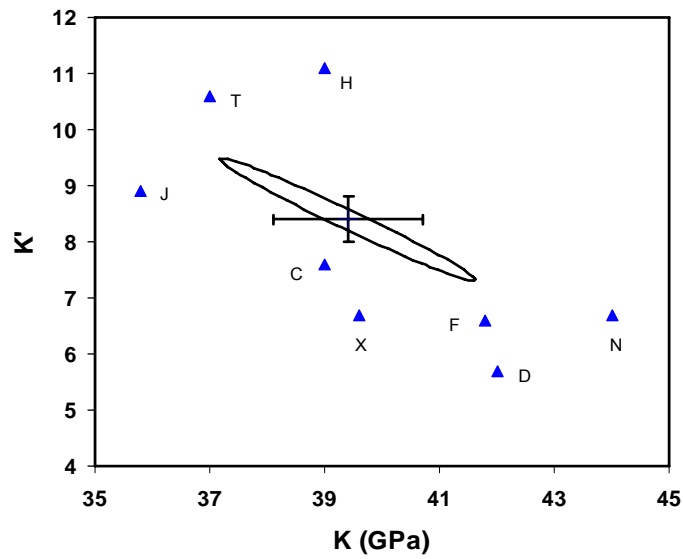


Figure 3.



(a)



(b)

Figure 4.

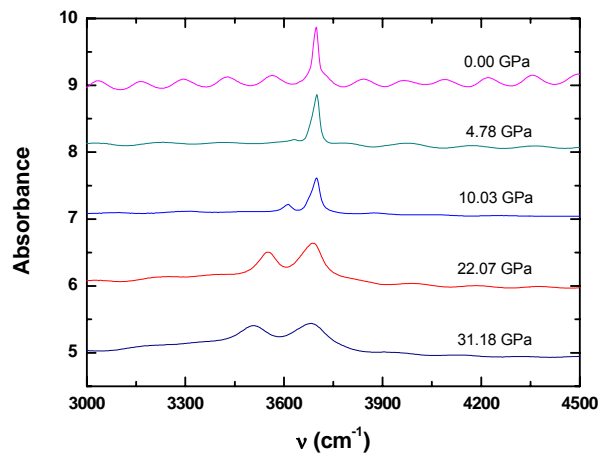
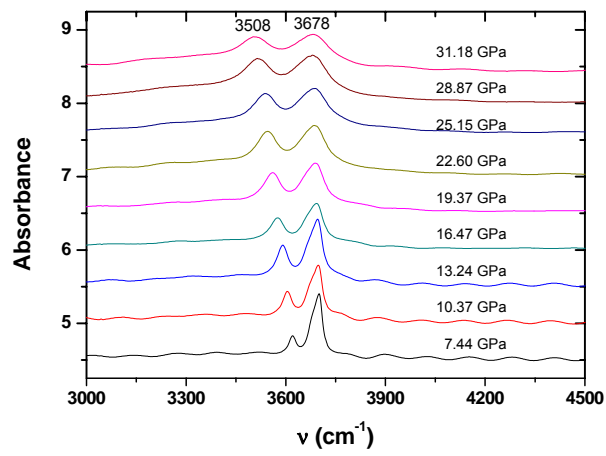
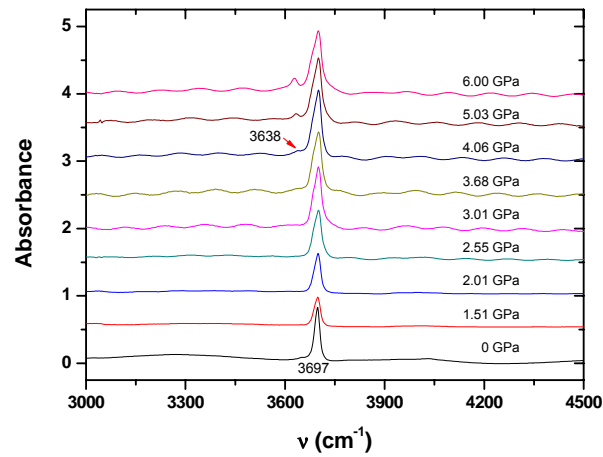


Figure 5.

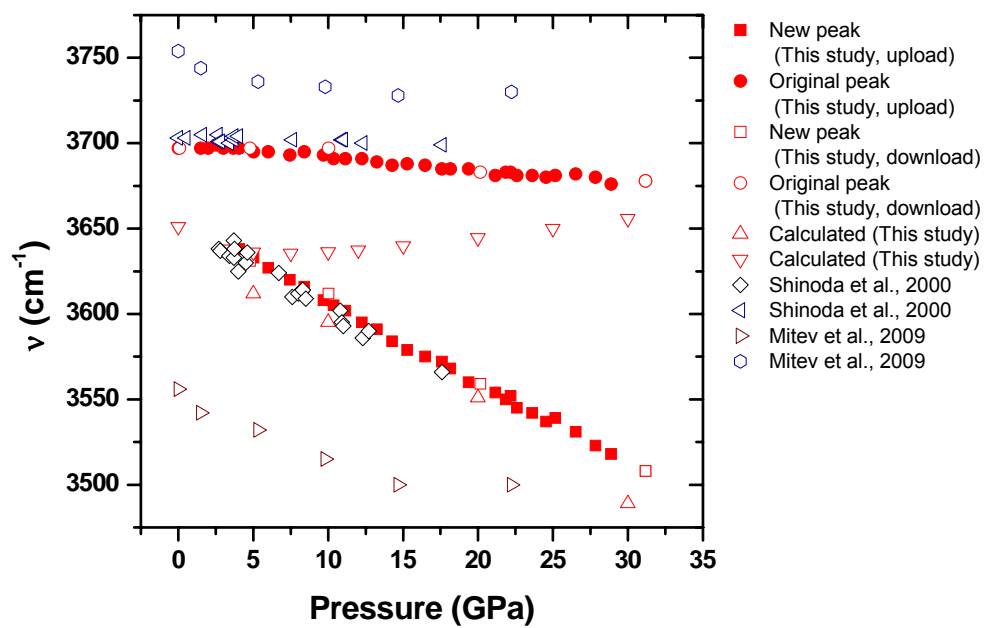
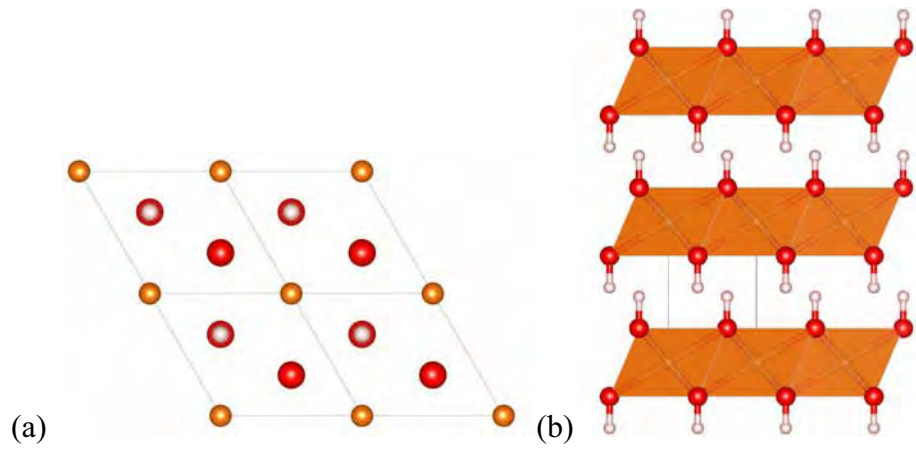


Figure 6.



(a)
Figure 1.

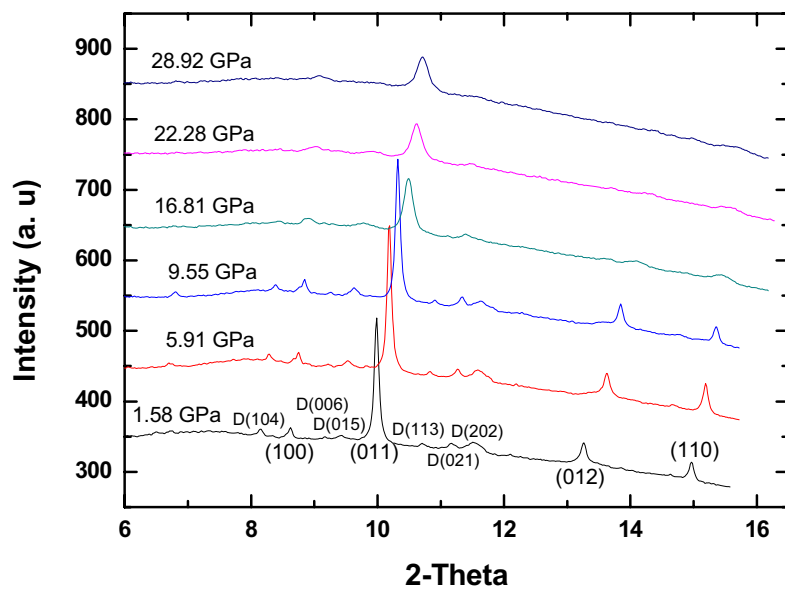


Figure 2.

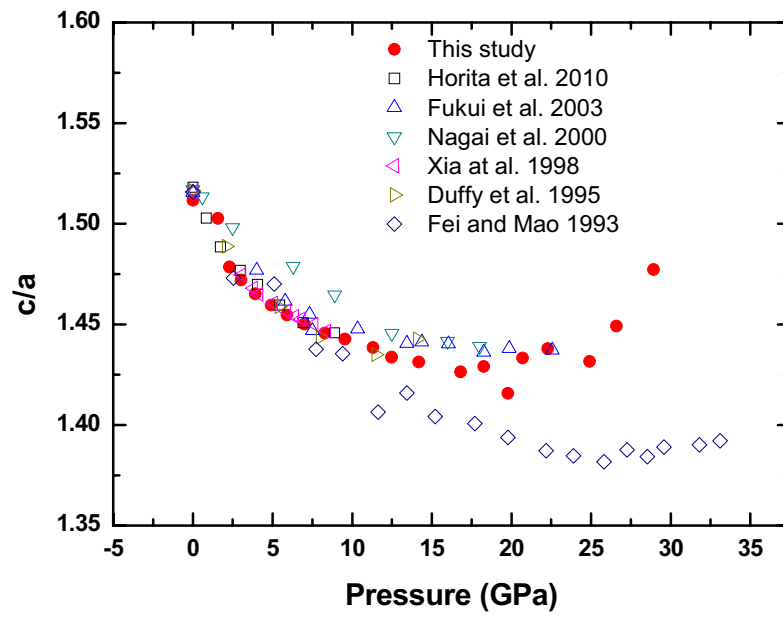
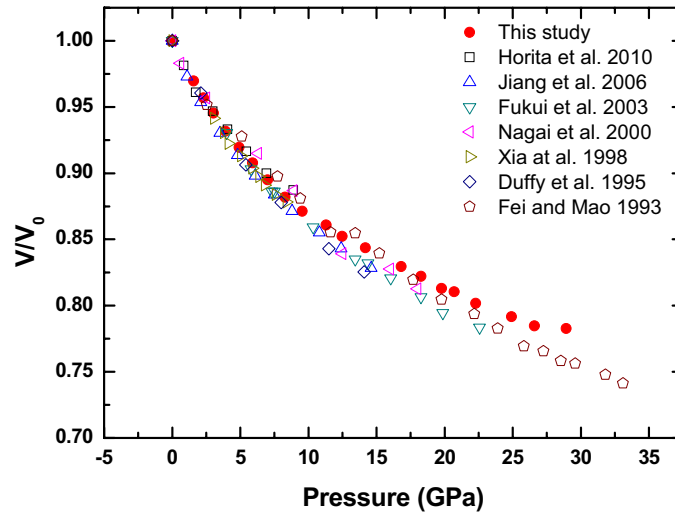
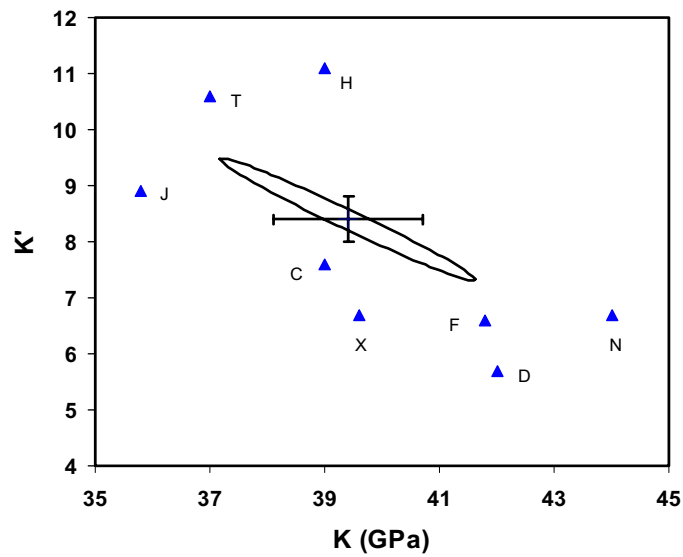


Figure 3.

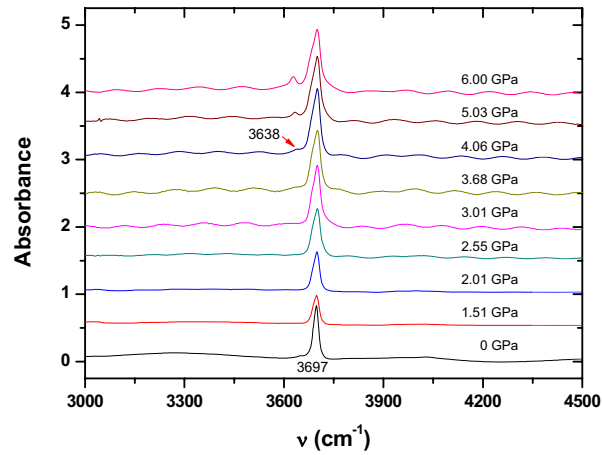


(a)

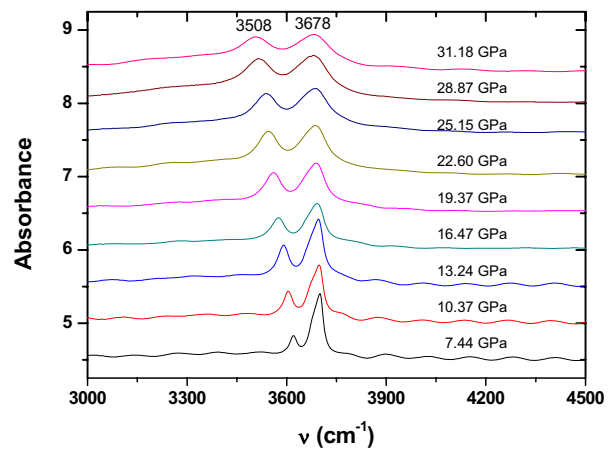


(b)

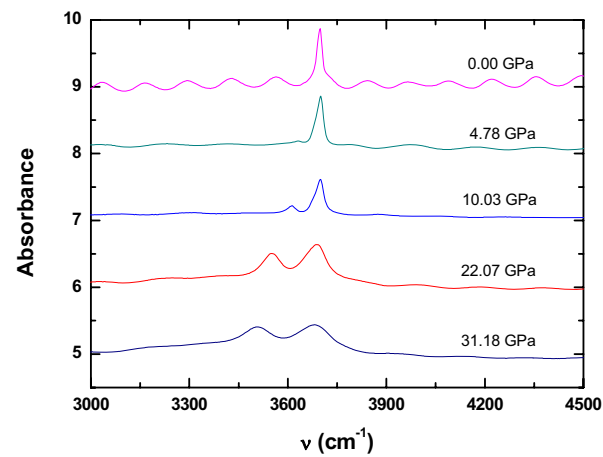
Figure 4.



(a)



(b)



(c)

Figure 5.

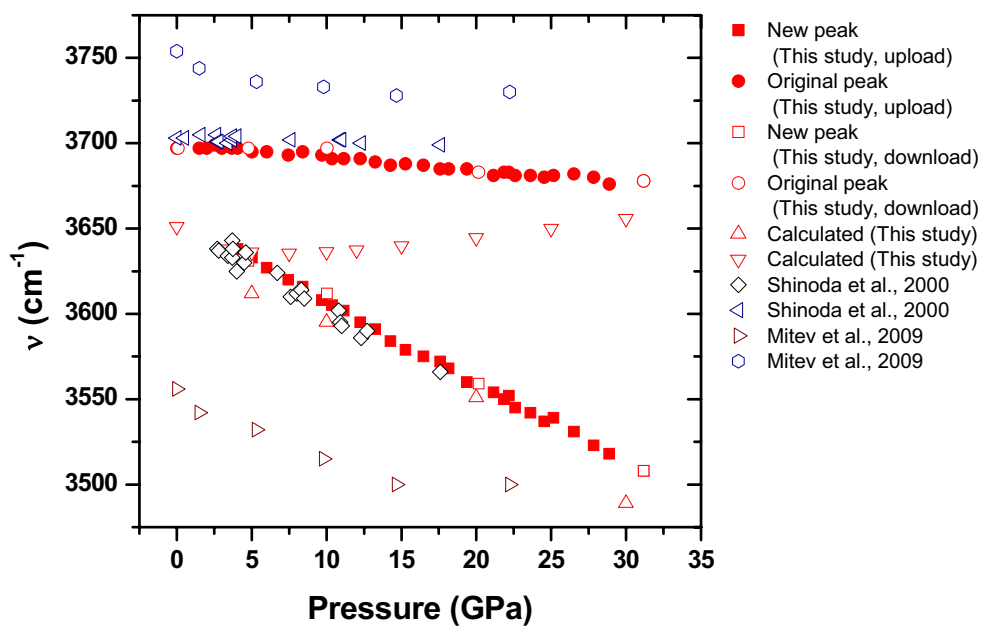


Figure 6.